Supporting Information

Enhanced Reactive Oxygen Species Generation and Pollutant Adsorption in Advanced Oxidation Processes via Ru Cluster-Oxygen Vacancy Synergy on BiOCl (111) Facet

Wensheng Zhang[a], Bo Ding[a], Zhishan Liang[a], Youlin Huang[a], Dongdong Qin[a], and Dongxue Han[a]*

[a]Center for Advanced Analytical Science c/o School of Chemistry and Chemical Engineering, School of Economics and Statistics, Guangzhou Key Laboratory of Sensing Materials & Devices, Guangzhou University, Guangzhou, Guangdong 510006, People's Republic of China.

*email: dxhan@gzhu.edu.cn

Supplementary Methods

Chemicals

Bismuth(III) nitrate pentahydrate ($Bi(NO_3)_3 \cdot 5H_2O$), potassium chloride (KCl), ruthenium(III) chloride ($RuCl_3$), and 5,5-dimethyl-1-pyrroline-N-oxide (DMPO) were purchased from Sigma-Aldrich Chemical Co. Ltd. Tetracycline hydrochloride (TC), isopropyl alcohol (IPA), and triethanolamine (TEOA) were obtained from Beijing InnoChem Technology Co. Ltd. All reagents were of analytical grade and were used without further purification.

Apparatus

The morphology and structure of the as-prepared catalysts were characterized using transmission electron microscopy (TEM, JEOL 2100F) and scanning electron microscopy (SEM, JEOL JSM-7001F). Crystalline phase identification was performed by powder X-ray diffraction (XRD) using a PANalytical X'Pert PRO diffractometer. Optical properties were analyzed through diffuse reflection spectroscopy (DRS) measurements on a HITACHI UV-3900 spectrophotometer. Surface chemical composition and electronic states were investigated by X-ray photoelectron spectroscopy (XPS) using a Thermo Scientific ESCALAB 250Xi system. Electrochemical properties were evaluated through Mott-Schottky measurements and electrochemical impedance spectroscopy (EIS) using CHI760-1 electrochemical workstation. The ultraviolet-visible absorption spectrum of TC was recorded on a Shimadzu UV-1800 spectrophotometer. The degradation intermediates of TC were identified by liquid chromatography-mass spectrometry (LC-MS, Agilent 1260-6460) operated in electrospray positive ion mode.

Electrochemical Tests

The electrochemical test was completed via a CHI760-1 electro-chemistry workstation (Shanghai Chenhua, China) with a three-electrode cell. The glass-carbon electrode loaded catalyzer was the work electrode, and the saturated Ag/AgCl electrode and platinum foil were the reference electrode and anti-electrode, separately. The transient photocurrent response curves were harvested during the illumination (on/off) every 20 s at an applied potential of 0 V (vs Ag/AgCl) in 0.1 M Na_2SO_4 solution from the back side of the work electrode. The electrochemical impedance spectroscopy (EIS) measurements were completed by using an AC voltage amplitude of 5 mV in the frequency range between 105 and 0.01 Hz in Na_2SO_4 electrolyte under open circuit potential (OCP) conditions and 300 W xenon light irradiation. The Mott−Schottky (M−S) plots were implemented with the electrochemical window ranging between -0.6 to +1.0 V, using 800 as well as an AC amplitude of 10 mV at each of the potentials.

Electron paramagnetic resonance (EPR) tests

The EPR technology was used to detect free radical species such as hydroxyl radical (·OH) and superoxide radical ($\cdot O_2^-$) with the assistance of 5,5-dimethyl-1-pyrroline N-oxide (DMPO). Briefly, for the detection of hydroxyl radical (·OH), the as-prepared sample was dispersed into deionized water to form a 2.5 mg mL^{-1} suspension under ultrasonic conditions. Subsequently, 50 μL DMPO was added into the above suspension under rapid stirring. Then, this mixture was irradiated for 5 min using a 300 W Xe lamp under the rapid agitation. After that, the supernatant of above mixture was quickly sampled and tested in the EPR equipment. Additionally, the detection procedure of superoxide radical ($\cdot O_2^-$) was the same as that of hydroxyl radical (·OH), except that the deionized water was replaced by methanol.

Optimization of light radiation intensity

The output of a 300 W xenon lamp was rigorously calibrated using a light radiometer (CEL-NP2000, Beijing China Education Au-light Co., Ltd.), with controlled and stable light irradiation intensities set at gradients of approximately 50, 80, 100, 150, and 200 mW·cm². Other experimental parameters, such as catalyst dosage, initial TC concentration, and reaction time, were kept consistent to systematically investigate the effect of light intensity on TC photocatalytic degradation. As shown in Fig. S3, the degradation efficiency of TC increases sharply as the light intensity rises from ~50 mW·cm² to ~100 mW·cm². This positive correlation is attributed to the enhanced generation of photo-induced electron-hole pairs. However, further increase to ~150 mW·cm² only resulted in minor improvements, indicating the possibility of reaching a state of "light saturation effect" (where the active sites on the catalyst surface are excessively occupied by photons, and additional photons cannot enhance the carrier generation efficiency), in which surface reaction kinetics become rate limiting. Continuing to increase the light intensity to ~200 mW·cm² may cause local overheating of the reaction system, leading to the aggregation of active sites on the catalyst surface such as Ru clusters, irreversible loss of OVs, or accelerated non targeted quenching of active free radical species, which in turn reduces degradation performance and increases energy consumption. Therefore, a light intensity of ~100 mW·cm² was determined as the optimal condition (also a commonly used value in our experimental system), ensuring a high reaction rate while maintaining energy efficiency.

Measurement of photocatalytic performances

The photocatalytic activity of the as-prepared photocatalysts was assessed by degrading TC in water. In brief, 20 mg of photocatalyst was placed in 100 mL of TC solution (50 mg L^{-1}). The above mixture was continually stirred in the dark for 30 min until it reaches equilibrium. Next, the photocatalytic process is conducted utilizing 300 W xenon lamp illumination (~100 mW·cm²) while being mechanically agitated. Then, the surplus photocatalyst was removed using filter paper after a tiny amount of the reaction solution was taken out at varied irradiation intervals. The upper

transparent layer was determined by recording the maximum absorbance of TC at 357 nm with a UV-visible spectrophotometer. Finally, the removal rate of TC was calculated using the following formula:

$$\eta_{\text{TC removal rate}}\,(\%) = (1 - C_t/C_0) \times 100\%$$

Where C_t is the TC concentration recorded during interval sampling as well as C_0 is the initial TC concentration.

Finite-Difference Time-Domain simulations

The Finite-Difference Time-Domain (FDTD) simulations were employed to describe the electric field distribution of nanostructures in this work. During the calculation, we set all x, y, z directions as perfectly matched layer boundary conditions. A total-field scattering-field plane wave was employed as the excitation light source. In addition, to obtain accurate calculation results in the future, we divided the simulation area into 0.2 nm × 0.2 nm × 0.2 nm mesh divisions. Its auto shoutoff min is set to 1×10^{-5} to ensure the convergence of the results.

Density functional theory (DFT) calculations

We employed first principles to conduct density functional theory (DFT) calculations. The Perdew Burke Ernzerhof (PBE) functional within the generalized gradient approximation (GGA) framework was utilized.[S1-S3] To precisely describe the ion-nucleus interaction, the projected augmented wave (PAW) potential was selected. For valence electrons, a plane-wave basis set with a kinetic-energy cutoff of 450 eV was adopted.[S4, S5] Additionally, to permit partial occupation of Kohn-Sham orbitals, the Gaussian smearing method was further implemented, with a smearing width set to 0.05 eV. During the self-consistency calculation of electron energy, the convergence

threshold for energy change was set to 10^{-5} eV. For geometric optimization, convergence was considered when the energy change was less than 0.05 eV $Å^{-1}$. To guarantee calculation accuracy, a vacuum spacing of 18 Å was set in the direction perpendicular to the structural plane. In the structural calculation, the integration over the Brillouin zone was performed using the 2 × 2 × 1 Monkhorst-Pack k-point sampling scheme. Finally, the preferential formation of different structures in BiOCl-Ru was evaluated by calculating the binding energy (E_b) of Ru clusters on different crystal facets of BiOCl:

$$E_b = E_{ad/sub} - E_{ad} - E_{sub}$$

Where $E_{ad/sub}$, E_{ad}, and E_{sub} are the total energies of the optimized adsorbate/substrate (i.e., Ru/BiOCl) system, the adsorbate (e.g., Ru clusters) in the structure, and the clean BiOCl substrate, respectively.

Additionally, we incorporated the Grimme DFT-D_3 method[S6] to accurately capture van der Waals interactions. The adsorption energy ($E_{ads.}$) of a gas/liquid phase molecule (e.g., O_2, H_2O, tetracycline) was determined by the formula:

$$\Delta E_{ads.} = E_{(surface + adsorbent)} - E_{(surface)} - E_{(adsorbent)}$$

Where $E_{(surface+adsorbent)}$, $E_{(surface)}$ and $E_{(adsorbent)}$ represented the energies of the molecule adsorbed on the surface, surface and molecules, respectively.

Supplementary Figures

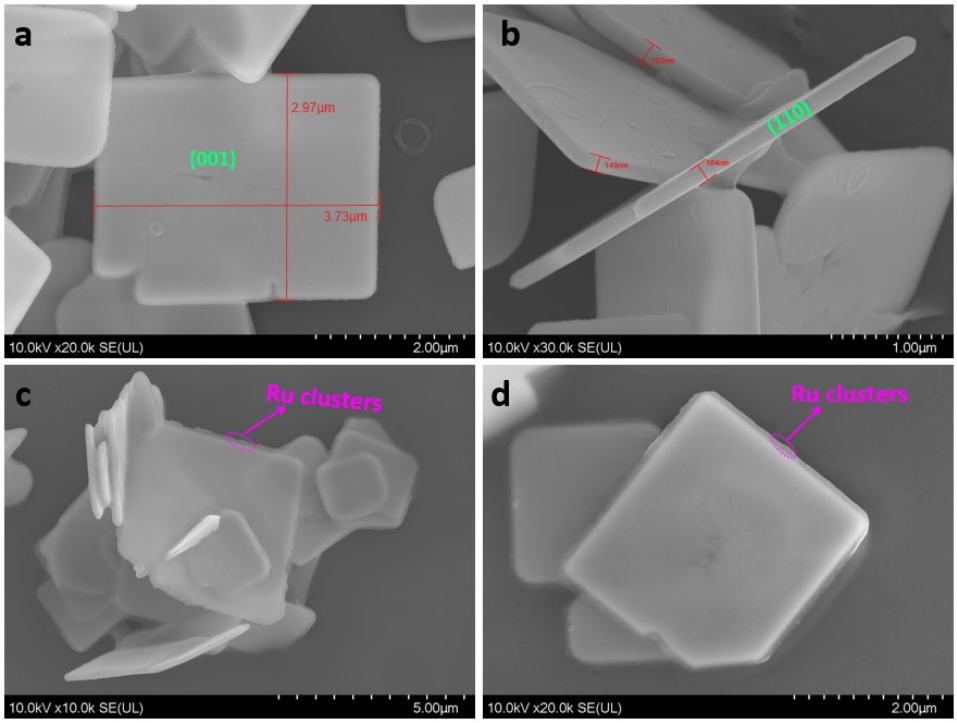

Fig. S1. SEM images of BiOCl nanoplates (a, b) and BiOCl-Ru (c, d) from different perspectives.

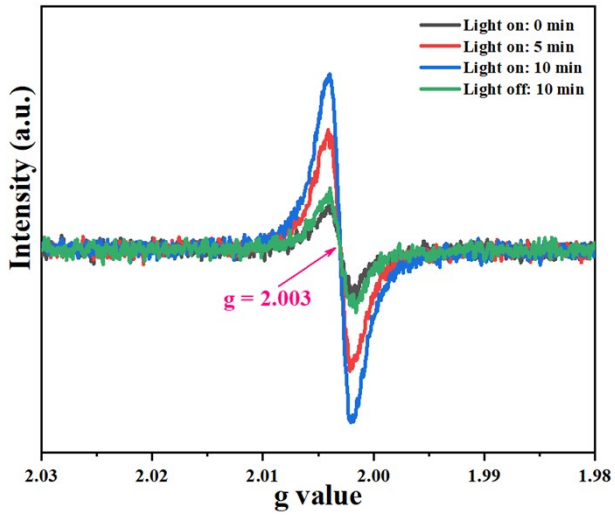

Fig. S2. The in situ EPR spectra correspond to the signals of the BiOCl-Ru sample before irradiation, after 5 min and 10 min of irradiation, and 10 min after the light is turned off.

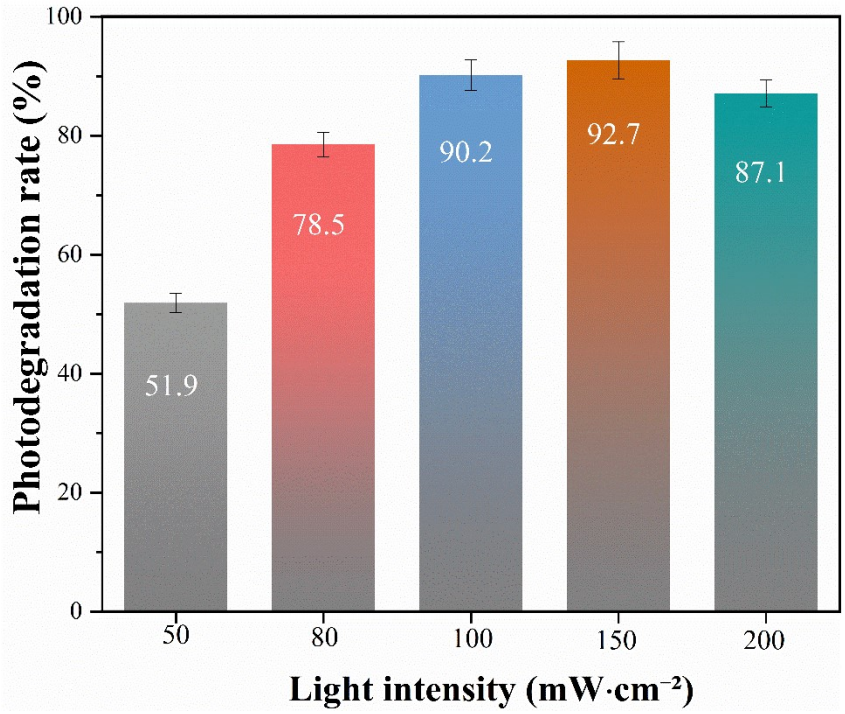

Fig. S3. Photodegradation activity of TC over BiOCl-Ru sample under different light intensities (after 75 min light irradiation).

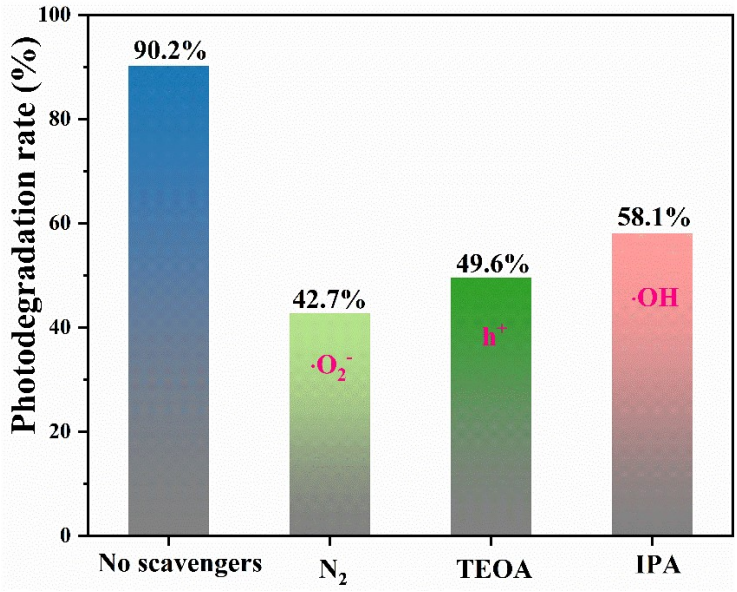

Fig. S4. Photocatalytic activities of TC over BiOCl-Ru with various scavengers.

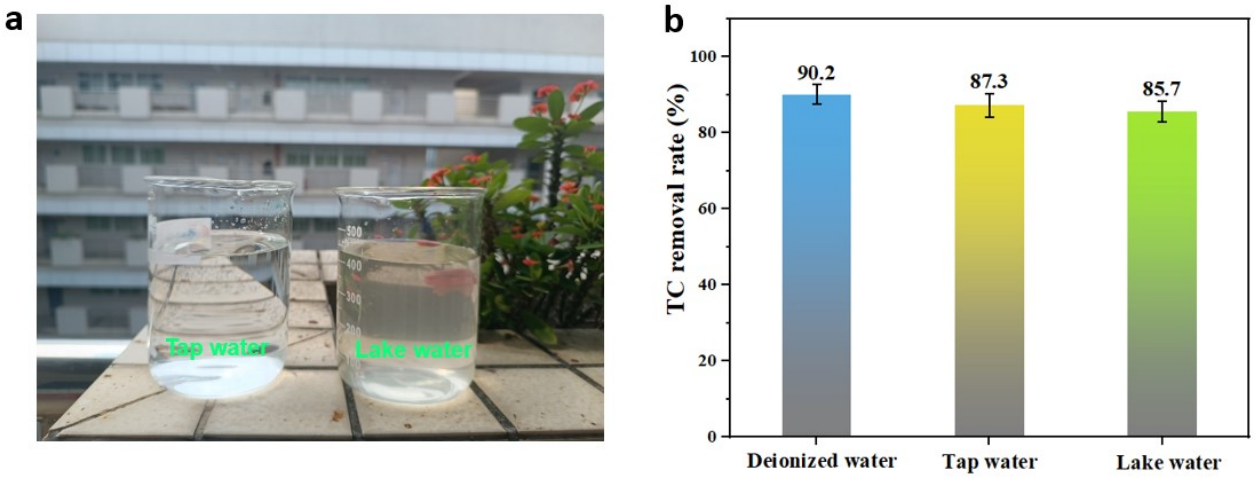

Fig. S5. (a) Photos of the as-collected water bodies (tap water and lake water); (b) Photocatalytic degradation of TC by BiOCl-Ru in different water quality.

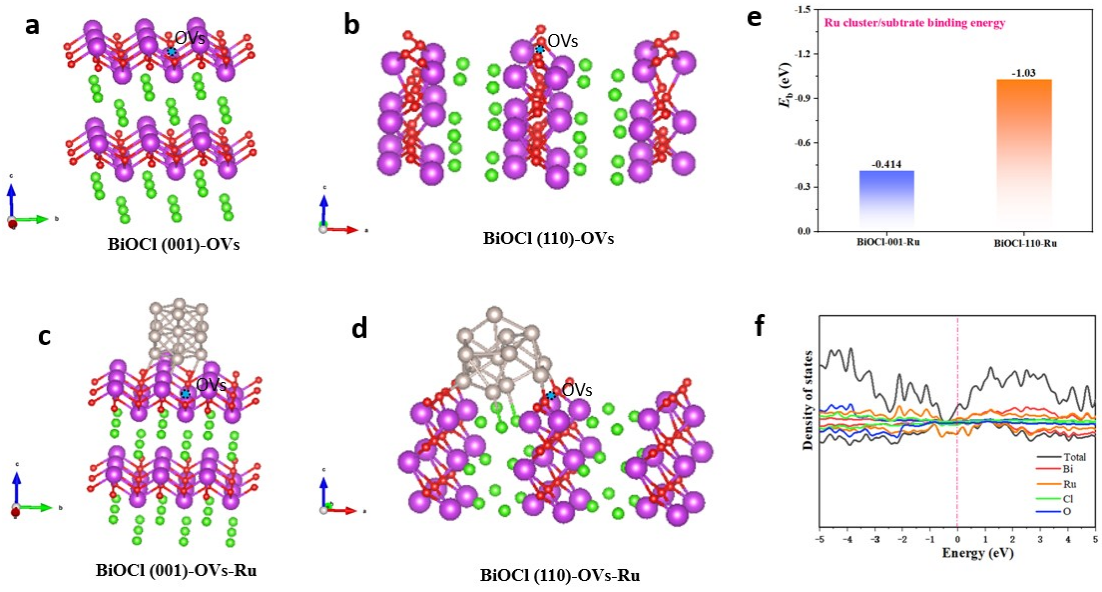

Fig. S6. The DFT-established model of (a) BiOCl with (001) facet, (b) BiOCl with (110) facet, (c) BiOCl (001)-OVs-Ru and (d) BiOCl (110)-OVs-Ru. (e) Binding energy of Ru cluster on different facets of BiOCl nanoplates. (F) TDOS calculation using the PBE method of BiOCl-Ru.

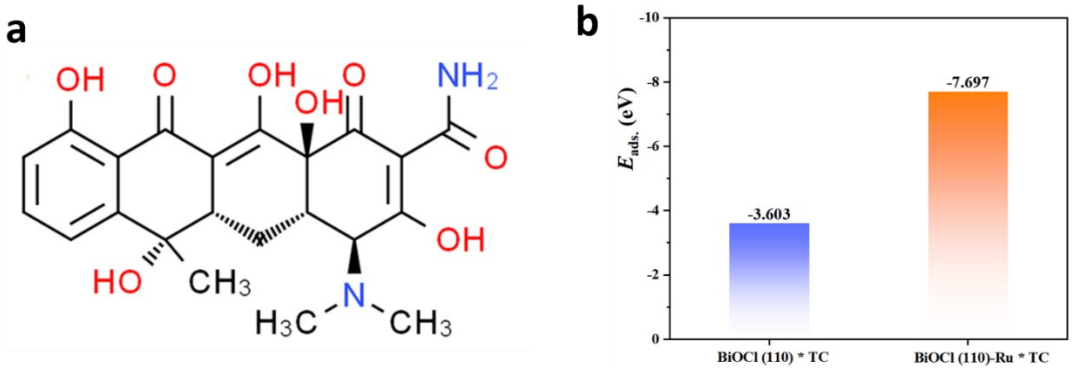

Fig. S7. (a) Molecular formula of tetracycline; (b) Adsorption energy of TC molecules adsorbed on BiOCl (110) and BiOCl (110)-Ru surfaces.

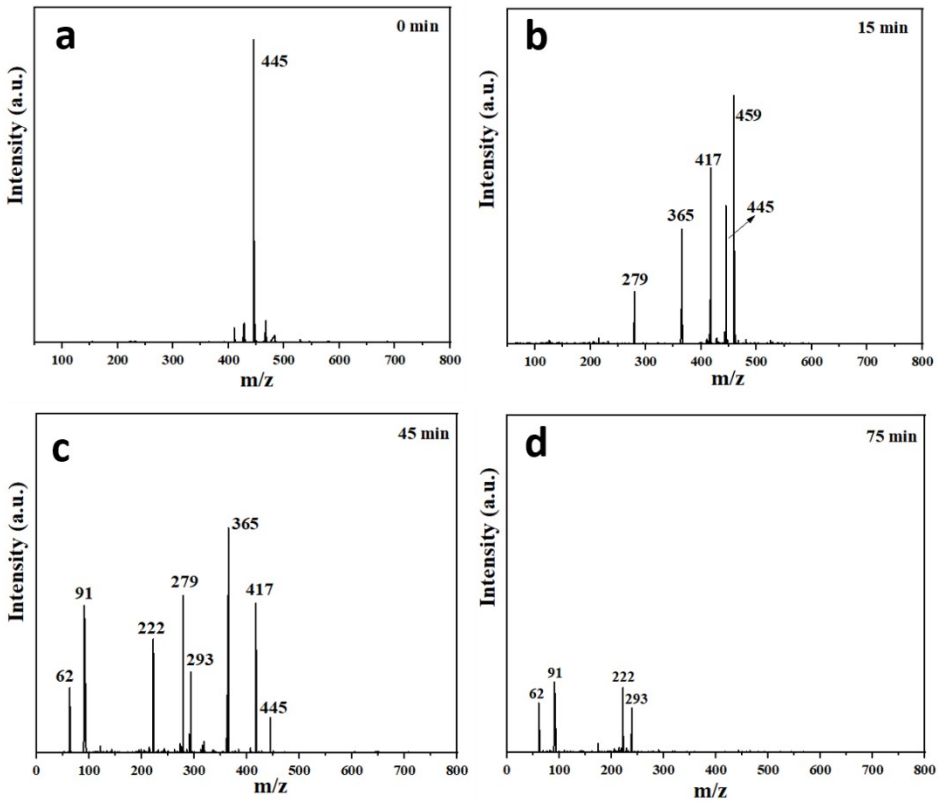

Fig. S8. LC-MS signals of degraded TC over BiOCl-Ru with different reaction time: (a) TC in 0 min, (b) degradation of TC in 15 min, (c) 45 min and (d) 75 min.

Supplementary Tables

Table S1. The content of Ru loaded on the BiOCl-Ru-x% samples was determined by ICP-OES.

Samples	BiOCl-Ru-0.5%	BiOCl-Ru-1%	BiOCl-Ru-2%	BiOCl-Ru-3%
Co (wt %)	0.47	0.93	1.89	2.82

Table S2. Comparison of photocatalysts toward the removal of TC.

Pollutants	Catalyst	Operating conditions	Degradation efficiency（k value）	Ref.
TC	BiOCl-Ru	initial concentration: 50 mg L^{-1} Catalyst dosage: 0.2 g L^{-1}	0.0279 min^{-1}	**This work**
TC	TiO_2/Bi_2O_3	initial concentration: 15 mg L^{-1} Catalyst dosage: 0.4 g L^{-1}	0.0165 min^{-1}	*J. Clean. Prod.,* 2022, 375, 134112.
TC	In_2Se_3	initial concentration: 20 mg L^{-1} Catalyst dosage: 0.5 g L^{-1}	0.0175 min^{-1}	*Appl. Catal., B,* 2020, 260, 118218.
TC	PS@TiO_2/Bi_2O_3-0.4	initial concentration: 50 mg L^{-1} Catalyst dosage: 0.2 g L^{-1}	0.03318 min^{-1}	Mater. Horiz., 2023, 10, 5869.
TC	Bi_2O_3 QDs/g-C_3N_4	initial concentration: 10 mg L^{-1} Catalyst dosage: 0.1 g L^{-1}	0.0144 min^{-1}	*Appl. Catal., B,* 2021, 295, 120279.
TC	WO_3/BiOBr/g-C_3N_4	initial concentration: 10 mg L^{-1} Catalyst dosage: 0.5 g L^{-1}	0.0264 min^{-1}	*J. Alloy. Compd.,* 2025, 1010, 177420.
TC	ABO-290	initial concentration: 40 mg L^{-1} Catalyst dosage: 0.3 g L^{-1}	0.013 min^{-1}	*Chem. Eng. J.,* 2022, 432, 134316.
TC	$InVO_4/ZnIn_2S_4$	initial concentration: 50 mg L^{-1} Catalyst dosage: 0.6 g L^{-1}	0.0186 min^{-1}	*Sep. Purif. Technol.,* 2025, 353, 128515.
TC	TCN-150	initial concentration: 20 mg L^{-1} Catalyst dosage: 0.25 g L^{-1}	0.0206 min^{-1}	*Chem. Eng. J.,* 2022, 432, 134375.

References

S1. G. Kresse, J. Furthmüller, Efficiency of ab-initio total energy calculations for metals and semiconductors using a plane-wave basis set. *Comp. Mater. Sci.,* 1996, ***6,*** 15–50.

S2. G. Kresse, J. Furthmüller, Efficient iterative schemes for ab initio total-energy calculations using a plane-wave basis set. *Phys. Rev. B,* 1996, ***54,*** 11169−11186.

S3. J. P. Perdew, K. Burke, M. Ernzerhof, Generalized gradient approximation made simple. *Phys. Rev. Lett.,* 1996, ***77,*** 3865−3868.

S4. G. D. Kresse, J. Joubert, From ultrasoft pseudopotentials to the projector augmented wave method. *Phys. Rev. B,* 1999, ***59,*** 1758−1775.

S5. P. E. Blöchl, Projector Augmented-Wave Method. *Phys. Rev. B,* 1994, ***50,*** 17953−17979.

S6. S. Grimme, J. Antony, S. Ehrlich, H. Krieg, A consistent and accurate ab initio parametrization of density functional dispersion correction (DFT-D) for the 94 elements H-Pu. *J. Chem. Phys.,* 2010, ***132,*** 154104.